Title: A Parametric Investigation on the Seismic Capacity of Masonry Cross Vaults

Angelo Gaetani[a,*], Paulo B. Lourenço[b], Giorgio Monti[c], Gabriele Milani[d]

[a] Postdoctoral Research Fellow, Department of Structural Engineering and Geotechnics, Sapienza University of Rome, Faculty of Engineering, 00184 Rome, Italy. Phone: +39 0644585405; Fax: +39 064884852; E-mail: angelo.gaetani@uniroma1.it

[b] Full Professor, ISISE, Department of Civil Engineering, University of Minho, Campus de Azurem, 4800-058, Guimarães, Portugal. Phone: +351 253510209; Fax: +351 253510217; E-mail: pbl@civil.uminho.pt

[c] Full Professor, Department of Structural Engineering and Geotechnics, Sapienza University of Rome, Faculty of Architecture, 00197 Rome, Italy. Phone: +39 0649919197; Fax: +39 0649919150; E-mail: giorgio.monti@uniroma1.it

[d] Associate Professor, Department of Architecture, Built environment and Construction engineering ABC, Technical University of Milan, 20133 Milano, Italy. Phone: +39 0223994290; Fax: +39 0223994220; E-mail: gabriele.milani@polimi.it

* Corresponding author

Abstract: Considering the relevance and the artistic value of cross vaults in European seismic prone areas, a parametric study on the seismic capacity of this element is presented. In particular, the behaviour of the so-called groin vault is discussed, i.e. intersection at a right angle of two semi-circular barrel vaults. The influence of span, rise, thickness, infill, and masonry tensile strength is investigated with respect to two boundary conditions, representative of typical vault configurations within heritage buildings. The analyses were performed using an upper bound approach of standard limit analysis. For the sake of clarity, the adopted code framework is briefly reviewed.

With the aim of identifying the most frequent failure mechanisms, the outcomes of the parametric analysis have been visually inspected and sorted according to the input parameters. Aiming towards a simplified assessment criterion, the resulting list of parameters was subsequently processed through multiple linear regression analyses that can help practitioners in quick seismic evaluation.

Keywords: cross vault, seismic capacity, limit analysis, failure mechanism, regression analysis.

1. Introduction

Masonry vaults represent one of the most important structural topologies within cultural heritage buildings. . In Europe, they were mostly developed during the Roman Empire and in the period between High Middle Ages and Renaissance, achieving such a level of beauty and technological perfection that still amazes the modern observer. However, despite the relevance and the long-lasting history, being conceived to withstand only gravitational loads, masonry vaults are threatened by seismic events. This has been emphasized by the systematic damage surveys carried out in churches and historical centres after recent Italian earthquakes [8,21–23]. In this regard, considering the limited research in the field, the present paper aims to investigate the seismic behaviour of cross vaults. The study focused on the so-called groin vault, the simplest kind of cross vaults, obtained by the intersection at a right angle of two semi-circular barrel vaults.

In order to illustrate the most frequent damages for cross vaults due to seismic action, it is worth referring to the Italian National Civil Protection Service [8]. By means of a systematic observation of the damages occurred during the strongest Italian earthquakes of the last 30 years, researchers have individuated the most recurring crack patterns for several elements of a church, regardless age, technology and dimensions of the constructions. In this regard, Figure 1 reports the crack patterns for cross vaults according to the location in the building.

The mechanism labelled as M7 regards the vaults of lateral aisles. The remarkable lower stiffness of the central nave colonnade with respect to the external wall produces a differential longitudinal displacement along the vault sides, i.e. an in-plane shear distortion, with the typical diagonal crack along the diagonal. On the other hand, mechanisms M8, M9, M12, M18, M24 regard the nave, lateral aisle, transept, apse (and presbytery) and chapels vaults, respectively. Support displacements (i.e. translation and rotation that can widen or narrow the vault span) and concentration of shear stresses are the main causes of damages. However, it is still not clear

how geometrical and mechanical features influence the vault failure, representing a relevant issue for seismic assessment.

In general, the parameters that affect the seismic behaviour of the vault are numerous, such as geometrical quantities, presence of ribs, connections, overall weight (and mass), previous strengthening measures (e.g. the old-fashioned concrete cap) or concentrated loads (e.g. roof truss resting on the extrados of the vault). The infill plays a crucial role too, as already pointed out for masonry arches [24–27], but also in the analysis of the two cross vaults of the Basilica of Assisi collapsed during the earthquake of Umbria and Marche in 1997 [28]. An excess of infill, in fact, may overload the vault and increment permanent vertical deformation, i.e. the vault reduces the original curvature, thus the bearing capacity.

In order to shed light on these aspects, this paper presents the results of a parametric analysis aimed at evaluating the influence of geometry, tensile strength and infill on the seismic behaviour of groin vaults. In particular, the ranges of vault dimensions (span, rise, thickness) were deduced from literature, from both historical [17] and experimental points of view [18–20]. The analyses basically focused on seismic capacity and failure mechanisms according to two different boundary conditions. The first regards fixed supports that induce an out-of-plane failure, in the fashion of a masonry arch undergoing horizontal action. This configuration is typical of supports with the same stiffness, e.g. vaults in the central naves. The second is aimed at modelling the in-plane shear distortion labelled as M7 in Figure 1. The effect of support settlements, discussed in [10–13], are not considered in the present work, as it focuses on seismic action.

Regarding the infill, its influence on arched structure is a delicate and still open issue. In case limit analysis and gravitational loads are considered, the influence of the infill on the behaviour of the vault may be taken into account indirectly through the vertical load corresponding to its self-weight, with or without load dispersal, e.g. [14,15] (a more detailed

discussion on this topic is reported in [16]). For the analyses of the present paper, the infill was modelled as distributed load and mass on the extrados of the vault. This approach neglects the proper distribution of vertical and horizontal pressure, the influence of its possible tensile strength (resulting from a loose material with low contents of some binding agent), and the nonlinear behaviour of the infill during motion (changes between active and passive pressure). Nonetheless, this approach is considered adequate for engineering applications.

The analyses were performed through a non-commercial code implemented by the last author. It is based on the kinematic theorem of standard limit analysis (with associated flow rule) and, although a concise review is reported next, the reader is referred to [4,29] for further details.

The results of the parametric analysis have been visually inspected and for each boundary condition it was possible to isolate a few main failure mechanisms, together with the relative range of input parameters. Relating this list of parameters to a multiple linear regression analysis provided a valuable tool for expedite seismic evaluation of groin vaults, which is a first step for addressing the lack of recommendations in current Codes of Practice, e.g. [5–7].

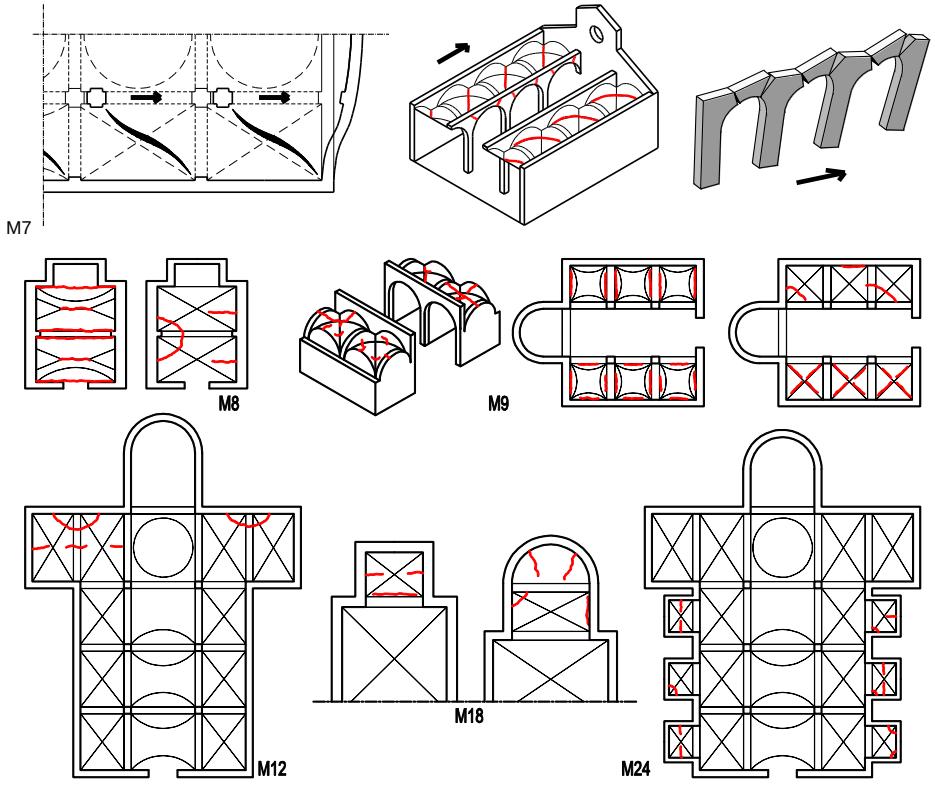

Figure 1. Cross vault mechanisms in churches [8,22]: M7 (longitudinal response of central nave colonnade) and M8, M9, M12, M18, M24 (nave, lateral aisle, transept, apse/presbytery and chapels, respectively)

2. Review of the adopted numerical code

The FE discretization of the groin vault was represented by means of rigid flat six-noded wedge elements. The utilization of wedges (i.e. 3D elements) instead of curved shell elements provides the possibility of adopting the same model in case of surface reinforcement with FRP strips (either at the intrados or extrados). Moreover, from the computational point of view, wedge elements require only in-plane and out-of-plane shear homogenized masonry failure surfaces, since flexural behaviour is derived at a structural level by integration along the thickness [4].

The wedges are assumed rigid infinitely resistant, implicitly assuring transverse sections to remain plane and the internal dissipation to be allowed only at the interfaces between neighbouring elements. More in detail, the kinematic variables for each wedge element *E* are represented by three centroid velocities $\left(u_x^G, u_y^G, u_z^G\right)$ and three rotations around centroid ***G***, (Φ_x^G, Φ_y^G, Φ_z^G), as reported in Figure 2a. The edge surface Γ_{12}^E, which connects P_1, P_2, P_4 and P_5 nodes, is rectangular and the jump of velocities on it is linear. In particular, the velocity field of a generic point ***P*** with global coordinates (x_P, y_P, z_P), on Γ_{12}^E is expressed in the global frame of reference as:

$$\mathbf{U}_{(P)} = \begin{bmatrix} u_x \\ u_y \\ u_z \end{bmatrix} = \begin{bmatrix} u_x^G \\ u_y^G \\ u_z^G \end{bmatrix} + \begin{bmatrix} 0 & -\Phi_y^G & \Phi_z^G \\ \Phi_y^G & 0 & -\Phi_x^G \\ -\Phi_z^G & \Phi_x^G & 0 \end{bmatrix} \begin{bmatrix} x_P - x_G \\ y_P - y_G \\ z_P - z_G \end{bmatrix} = \mathbf{U}_E^G + \mathbf{R}_E(\boldsymbol{P} - \boldsymbol{G}) \qquad (1)$$

where $\mathbf{U}_{(P)}$ is the point *P* velocity, $\mathbf{U}_E^G$ is the element *E* centroid velocity and $\mathbf{R}_E$ is the element *E* rotation matrix. From Equation (1), the jump of velocities $\left[\mathbf{U}_{(P)}\right]$ at a point *P* on the interfaces *I* between two contiguous elements *N* and *M* can be evaluated as the difference between the velocities of *P* belonging, respectively, to *N* and *M*:

$$\left[\mathbf{U}_{(P)}\right] = \mathbf{U}_M^G - \mathbf{U}_N^G + \mathbf{R}_M(P - G_M) - \mathbf{R}_N(P - G_N) \tag{2}$$

Denoting $\mathbf{R}^I$ as the rotation matrix with respect to the global coordinate system, the jump of velocities may be written in the local system (Figure 2b) as follows:

$$\left[\widetilde{\mathbf{U}}_{(P)}\right] = \begin{bmatrix}\Delta r_1 \\ \Delta r_2 \\ \Delta s\end{bmatrix} = \mathbf{R}^I\left[\mathbf{U}_{(P)}\right] \tag{3}$$

where Δr_1, Δr_2 and Δs are velocities jumps (two tangential and mutually orthogonal, and one perpendicular to the interface). Once the jump of velocities in the local frame of reference is known, it is possible to evaluate the power dissipated on a generic interface I of area Ω_{12} as follows:

$$\pi_{int} = \int_{\Omega_{12}} \left[\widetilde{\mathbf{U}}_{(P)}\right]^T \boldsymbol{\sigma}_{(P)} d\Omega = \int_{\Omega_{12}} (\Delta r_1 \tau_1 + \Delta r_2 \tau_2 + \Delta s\, \sigma_s)\, d\Omega \tag{4}$$

where $\boldsymbol{\sigma}_{(P)}^T = [\tau_1, \tau_2, \sigma_s]$ represents the stress vector acting at P on element M, in local stress coordinates (Figure 2b).

Regarding the masonry failure surface, as experimental evidences show, the basic failure modes for masonry walls with weak mortar are sliding along the joints, direct tensile splitting of the joints, and compressive crushing at the interface. These modes may be gathered adopting a Mohr-Coulomb failure criterion combined with a tension cut-off and a cap in compression [3].

Aiming at treating the problem within the framework of linear programming, a piecewise linear approximation of the failure surface is adopted. A homogenized strength domain $\phi = \phi(\boldsymbol{\sigma})$ in the local coordinate system $(\boldsymbol{\tau_1}, \boldsymbol{\tau_2}, \boldsymbol{\sigma_s})$ and constituted by m planes is supposed. Such a linearization for each interface (and, in principle, for each point of the interface) can be obtained applying the procedure recommended by Krabbenhoft et al. [30], and the reader is referred there for further details.

In particular, a generic linearization plane q has equation ϕ^q: $\boldsymbol{A}^{q^T}\boldsymbol{\sigma} = A^q_{\mathrm{r}1}\tau_1 + A^q_{\mathrm{r}2}\tau_2 + A^q_{\mathrm{s}}\sigma = C^q$, where $1 \le q \le m$ is assumed. Adopting the normality rule and introducing plastic multiplier rates $\dot{\lambda}^q_{(P)}$ (one for each linearization plane), the jump of velocity $\left[\widetilde{\boldsymbol{U}}_{(P)}\right]$ field is given by:

$$\left[\widetilde{\boldsymbol{U}}_{(P)}\right] = \sum_{q=1}^{m} \dot{\lambda}^q_{(P)} \frac{\partial \phi^q}{\partial \boldsymbol{\sigma}} \tag{5}$$

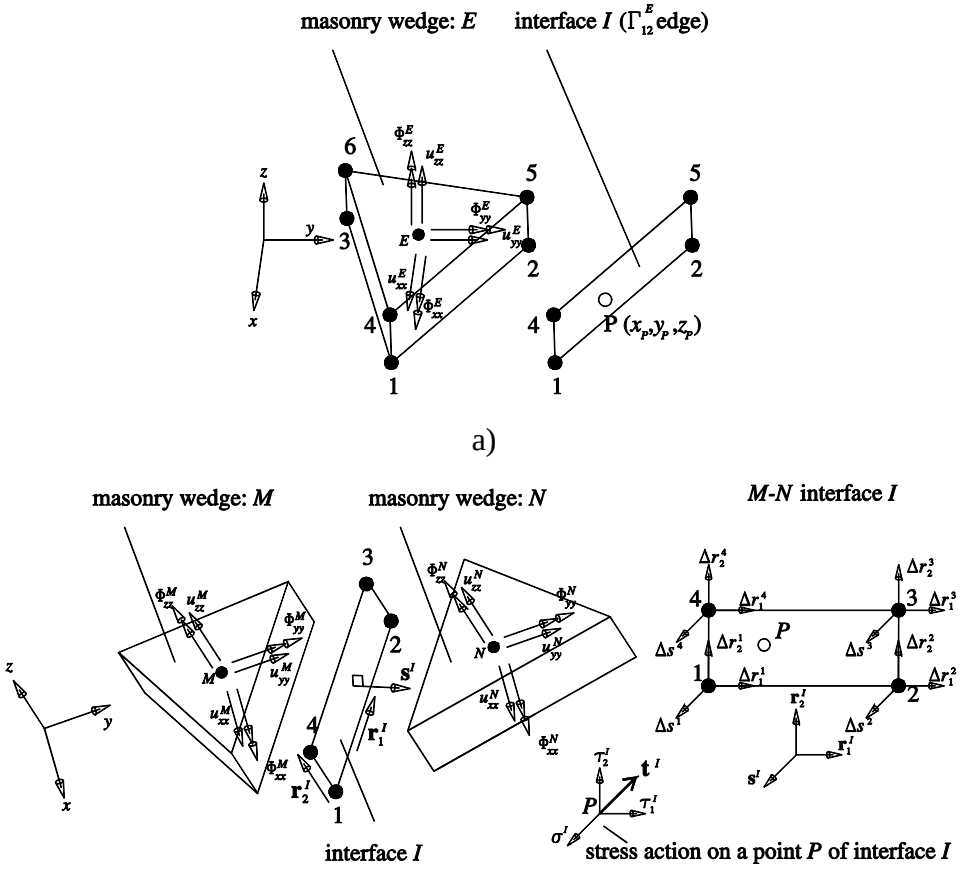

Figure 2. Masonry element discretization: a) six-noded wedge and four-noded interface; b) contiguous masonry elements (global and local frame of reference), from Milani et al. [4]

In order to solve Equation (4), since the jump in velocity on interfaces is assumed to vary linearly, e.g. Equation (3), it is necessary to evaluate Equation (5) only in correspondence of three different positions $P_k = (x_k, y_k, z_k)$ on *I*. Therefore, from Equations (4) and (5), the internal power dissipated on the generic interface *I* is expressed by:

$$\pi_{int} = \int_{\Omega_{12}} \left[\tilde{\mathbf{U}}_{(P)}\right]^T \boldsymbol{\sigma}_{(P)} d\Omega = \int_{\Omega_{12}} \sum_{q=1}^{m} \dot{\lambda}^q_{(P)} \left[\frac{\partial \phi^q}{\partial \boldsymbol{\sigma}}\right]^T \boldsymbol{\sigma}_{(P)}\, d\Omega$$
$$= \frac{\Omega_{12}}{3} \sum_{q=1}^{m} C^q \sum_{k=1}^{3} \dot{\lambda}^q_{(P_k)} \tag{6}$$

where all the symbols have already been introduced. It is interesting to notice from Equation (6) that the internal power dissipation depends on the plastic multiplier rates of points P_k only.

Moving to the global scale, the seismic loads have been simulated by introducing horizontal inertial forces proportional to the masses. The proportionality constant at collapse λ (load multiplier) gives the value of the force that lead the vault to failure. Accordingly, the external power dissipation can be written as:

$$\pi_{ext} = (\mathbf{P}_0^T + \lambda \mathbf{P}_1^T)\mathbf{w} \tag{7}$$

where $\mathbf{P}_0$ is the vector of permanent loads, $\mathbf{P}_1$ is the vector of seismic loads (dependent on load multiplier) and $\mathbf{w}$ collects the elements centroid velocities. As the amplitude of the failure mechanism is arbitrary, a further normalization condition $\mathbf{P}_1^T\mathbf{w} = 1$ is usually introduced. Hence, the external power becomes linear in $\mathbf{w}$ and λ and can be written as $\pi_{ext} = \mathbf{P}_0^T\mathbf{w} - \lambda$.

After some elementary assemblage operations, where the objective function is the total internal power dissipated minus the power dissipated by external loads, not dependent on the load multiplier, a linear programming problem is obtained, as:

$$\begin{cases} \lambda = \min_{\hat{\boldsymbol{x}}} \left\{ \sum_{I=1}^{n} \pi_{int} - \mathbf{P}_0^T \mathbf{w} \right\} \\ \mathbf{P}_1^T \mathbf{w} = 1 \\ \left[\widetilde{\boldsymbol{U}}_{(P_k)} \right] = \sum_{q=1}^{m} \dot{\lambda}_{(P_k)}^{q} \dfrac{\partial \phi^q}{\partial \boldsymbol{\sigma}} \\ \mathbf{U}_{(P_k)} = \overline{\mathbf{U}} \end{cases} \tag{8}$$

where n is the total number of interfaces and $\hat{\boldsymbol{x}}$ is the vector of total optimization unknowns (i.e. elements centroid velocities ($\mathbf{w}$) and rotations ($\boldsymbol{\Phi}$), and interface plastic multiplier rates). The constraints represent, respectively, normalization conditions, constraints for plastic flow in velocity discontinuities, and velocity boundary conditions (assigned velocity $\overline{\mathbf{U}}$).

Several linear programming tools suited for solving Equation (8) are available in literature. However, according to the characteristics of the present problem, which is large and sparse, the barrier method of the CPLEX was chosen as the best tool. This method is available in TOMLAB®, which is a modelling platform for solving applied optimization problems in Matlab. Moreover, since only some of the unknown variables are required to be integers, the problem was addressed as a mixed integer linear programming (MILP) problem. For more details, the reader is referred to specific literature, e.g. [31,32].

3. Analysis overview

3.1 Boundary conditions and geometry

The groin vault was studied considering two boundary conditions, named according to the type of failure, which are out-of-plane failure and in-plane shear distortion (Figure 3). The former is relevant to supports of comparable stiffness that, providing a rather large rigidity (horizontal displacements $u_{A,\,B,\,C,\,D} = 0$ and vertical displacements $v_{A,\,B,\,C,\,D} = 0$), make the vault fail in the fashion of an arch undergoing horizontal actions (e.g. vaults of central naves). The latter, instead, represents the typical failure produced by the large difference in stiffness

between two opposite sides of the vault, i.e. in-plane horizontal shear distortion (e.g. vaults of lateral aisles). Moreover, looking at Figure 3, in order to avoid an unrealistic spreading of the (corner) supports due to gravitational and seismic loads, the sliding supports were constrained to have the same horizontal displacement ($u_A = u_B \neq 0$).

In both cases, the present study addresses only the local behaviour of the vault, neglecting the real stiffness of the supporting elements or mutual interactions with the rest of the structure.

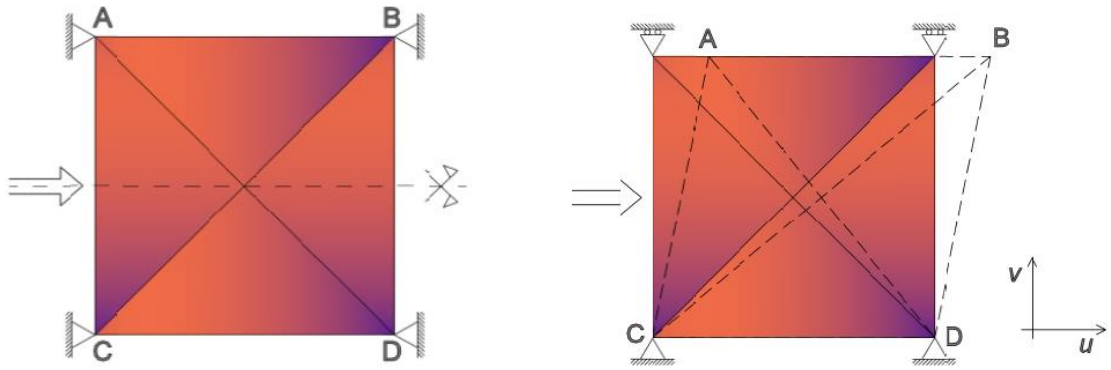

Figure 3. Plan view and boundary conditions, namely, a) out-of-plane failure and b) in-plane shear distortion

On the other hand, given the importance of geometry in the capacity of the vault, all the descriptive parameters of the geometry have been considered, namely angle of embrace (or arc of embrasure, which is the angle created by the two lines extending from the centre point of the defining arc to the springing point of each side of the arch / vault), diameter and thickness. In particular, in order to account for a reasonable range of vault dimensions, three values per each geometrical parameter were chosen: angle of embrace (120°, 130°, 140°), diameter (3.6, 4.5, 5.4 m), thickness/diameter ratio (1/20, 1/33, 1/50). The range of geometrical parameters was assumed based on both ancient rules of thumbs, exhaustively illustrated in Gaetani et al. [17], and geometries considered in several experimental investigations [18–20]. For instance, Rossi et al. [18] investigated the behaviour of a groin vault with a diameter of around 3.4 m, thickness of 0.12 m (that is, thickness/diameter ratio equal to 1/28) and angle of embrace of around 120°.

3.2 Infill as assigned load and mass

Four different levels of infill were considered in the present study. According to Figure 4, they are indicated by central angles equal to 0°, 40°, 60°, 90°, where 0° conventionally stands for no infill, while 90° represents the case in which the vault is completely covered.

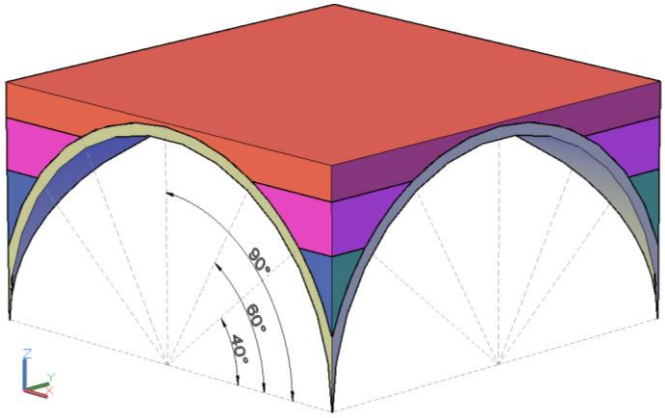

Figure 4. Infill levels according to the central angle

In order to evaluate its effects on the overall behaviour of the vault, the infill has been modelled as distributed load (and mass) on the extrados surface of the vault. According to Clemente's approach [33], Figure 5 shows the four schematizations adopted in the present study, where q_v and q_h represents the dead and horizontal load, where the former is the weight of the infill above the vault. Regarding the latter, assuming the seismic loads towards the right hand side, as follows: *I1*) q_h is equal to the contribution of horizontal stripes on the left side only; *I2*) as *I1* but on both sides; *I3*) $q_h = q_v$ on both sides; *I4*) the infill contribution is regarded as an overall distributed horizontal load, whose resultant is equal to the entire weight of the infill.

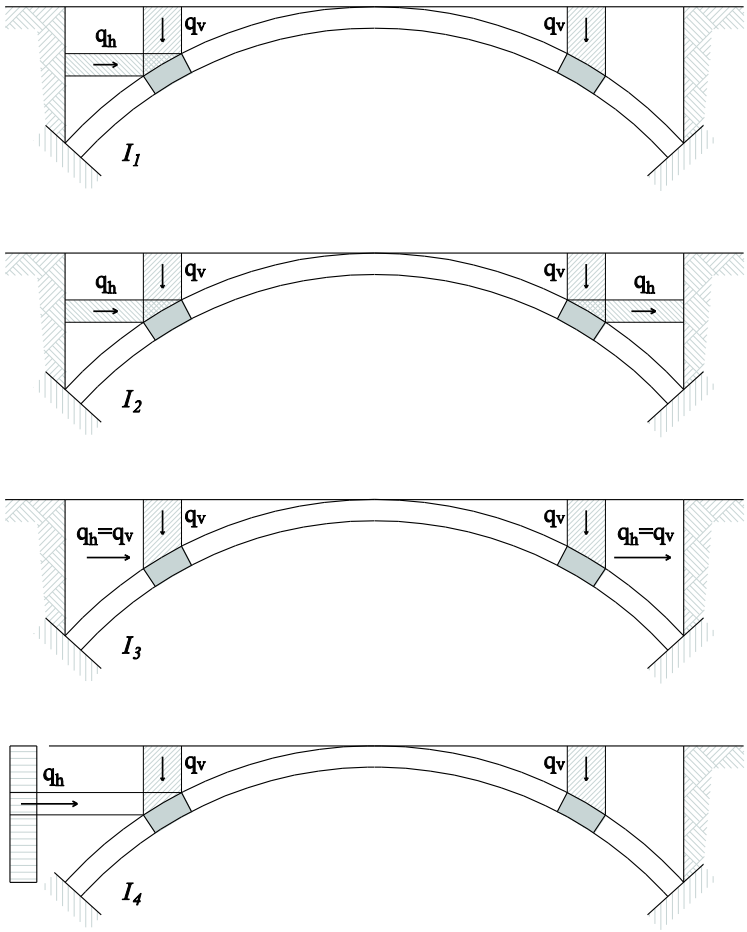

Figure 5. Schematization of the infill load/mass according to Clemente [33]

3.3 Numerical model

As far as mass density and compression strength are concerned, the properties implemented in the numerical model are in line with the values proposed in the Italian Codes of Practice [5,6]. In particular, the average values recommended for good stone masonry and brick masonry with lime mortar are adopted and reported in Table 1. Moreover, according to section 2, Table 1 shows also the piecewise linearized failure criterion adopted in the present study (proposed by Lourenço and Rots [3]) in terms of stresses normal (σ_{33}) and tangential to the interface plane (σ_{13}, σ_{23}). Consequently, the orthotropic behaviour of masonry is automatically taken into account simply defining the interface orientation.

In this regard, it is worth noticing that, according to Page [2], masonry anisotropy in compression for regular patterns is moderate due to the much higher strength of the blocks compared to the mortar. Dealing with masonry vaults, in particular, they usually fail under horizontal loads with the formation of plastic hinges, a situation where masonry compressive strength is rarely relevant. Accordingly, in the present investigation the compressive strength has been considered isotropic, independent of the direction of compressive stresses.

Finally, regarding cohesion, friction angle, and compression linearized cap angle (stiffness is not relevant in limit analysis), the values reported in Table 1 are widely adopted in literature. On the other hand, since tensile strength is considered to be the most influential parameter in the structural behaviour [9], three values were considered (0.05, 0.10, 0.20 MPa, of which the minimum was assumed of null strength).

Given the assumption of rigid-infinitely resistant blocks, the interfaces represent the place were fractures can occur. As a consequence, the mesh discretization assumes a crucial role in the description of the vault behaviour. Accordingly, starting with the directions of directrix and

generatrix of the web, the mesh was refined to accommodate more general fracture mechanisms (Figure 6).

A total of 2106 analyses were performed. For the sake of clarity, the parameters and the relative ranges are summarized as follows: three angles of embrace (120°, 130°, 140°), three diameters (3.6, 4.5, 5.4 m), three thickness/diameter ratios (1/20, 1/33, 1/50), two boundary conditions, four schematizations for the infill (Section 3.2), four levels of infill (0, 40°, 60°, 90°), three values of tensile strength (0.05, 0.10, 0.20 MPa).

As two different boundary conditions are involved (refer to Section 3.1), which lead to out-of-plane and in-plane failure mechanisms (1053 analyses each), the results are split and presented next.

Mass density sound masonry	ρ_s	1.8 ton/m^3
Mass density loose masonry (infill)	ρ_l	1.2 ton/m^3
Compression strength	f_c	3.2 MPa
Tensile strength	f_t	0.05, 0.10, 0.20 MPa
Cohesion	c	1.5 f_t
Friction angle	Φ	30°
Compression linearized cap angle	Φ_2	60°

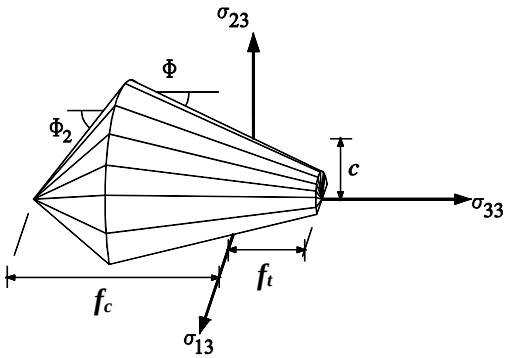

Table 1. Mechanical parameters adopted and piecewise linear approximation of the failure criterion [3]

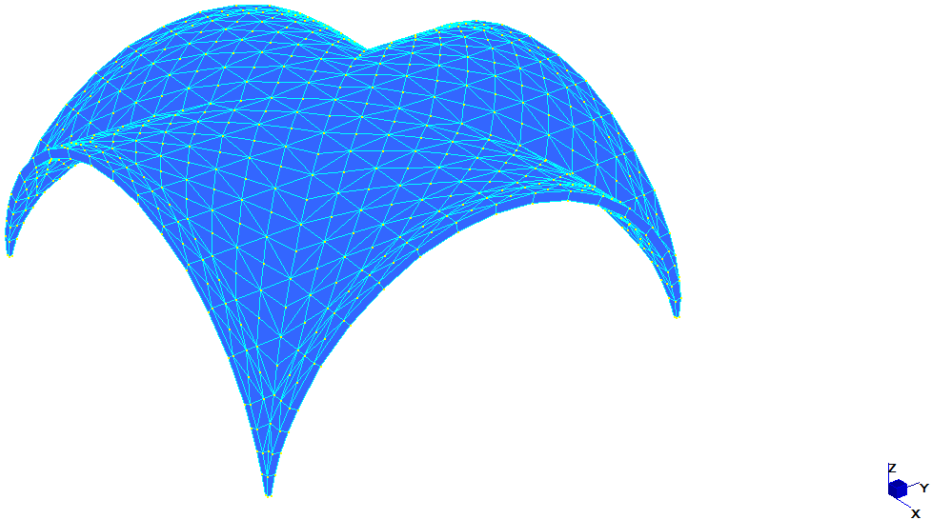

Figure 6. Mesh discretization adopted (thickness/diameter ratio equal to 1/50)

4. Out-of-plane failure

Given the approaches chosen to model the infill (see Figure 5), the initial study was aimed at evaluating the most conservative one, that is the one providing the lowest load multipliers in the largest number of cases. In this regard, *I2* resulted the most conservative schematization and, in the subsequent discussion, only these results are considered.

4.1 Failure mechanisms

The visual inspection of the resulting 324 analyses (243 with and 81 without infill) shed light on the most frequent mechanisms that, given the wide range of the input parameters, can be regarded as the most plausible ones for the out-of-plane failure. However, it must be underlined that larger values of tensile strength lead to more discernible mechanisms and different cases occasionally showed common features.

Table 2 collects the results in terms of occurrence frequency, where "null capacity" indicates the vaults that, according to the given parameters, did not exhibit any seismic capacity. Figure 7 shows the magnified deformed shape of the mechanisms with larger frequency. Due to the symmetry of the problem, the analogy with the arch is evident and, consequently, it is possible to schematize the cross vault behaviour according to simple kinematic configurations, i.e. single degree of freedom (SDOF) unstable scheme, for an arch. These are also reported in Figure 7, where the arrangements of the hypothetical constraints give the name to the mechanisms. Moreover, the constraints provide information about the cracks would possibly occur. For instance, hinges are located at either the intrados or extrados and the consequent opening leads to cracks evident only on the opposite face; on the other hand, rollers indicate a crack that goes through the entire thickness creating a sliding interface.

As it is possible to notice in Figure 7, when compared to an arch, an important role in the definition of the deformed shape is played by the orthogonal webs, which provide a larger flexural rigidity (e.g. a folded paper sheet). This feature prompts the inner hinges to be located in the central part of the vault (±20° from the crown line), where the rigidity is minimal.

Mechanisms	**Abbr.**	**Frequency**
Four hinges	**4H**	49%
Two hinges and roller	**2H&R**	20%
Roller and two hinges	**R&2H**	17%
Two rollers	**2R**	6%
Null capacity	**Null**	5%
Others	**-**	<3%

Table 2. Mechanism occurrence frequency for groin vaults undergoing out-of-plane failure

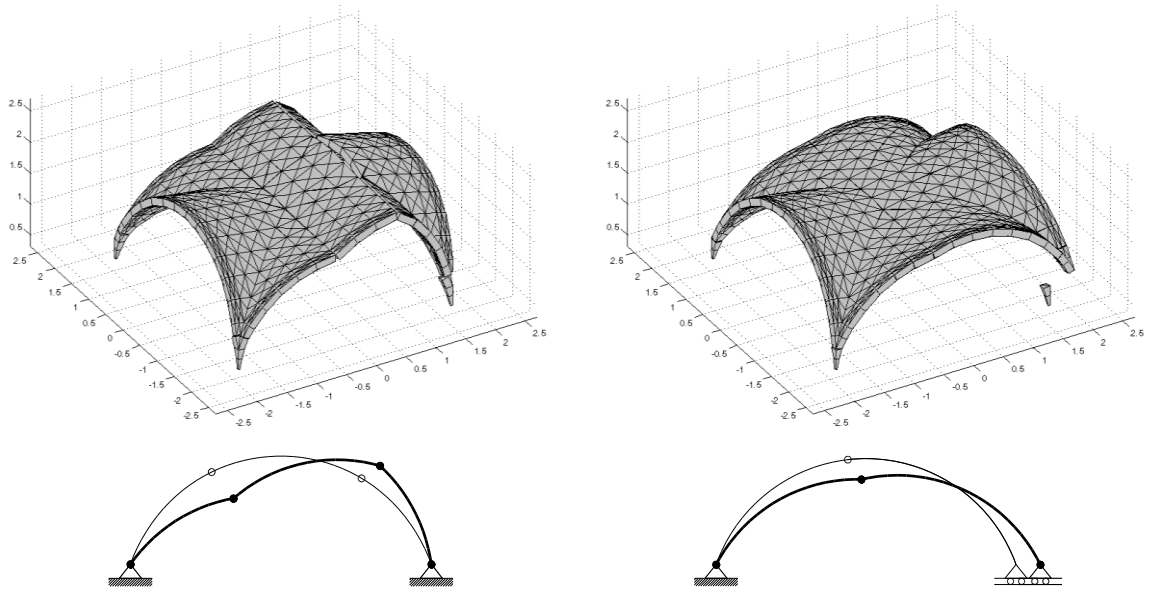

4H 2H&R

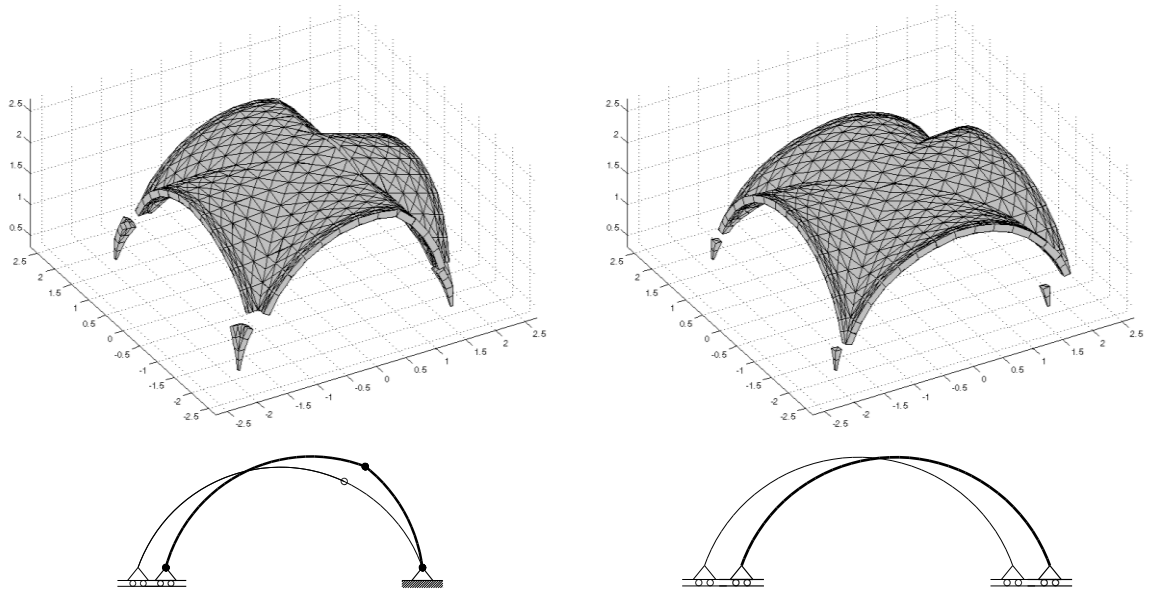

R&2H 2R

Figure 7. Most frequent mechanisms for out-of-plane failure and related schematization

For the given geometrical features, it is possible to compare the damage pattern of 4H depicted in Figure 7 with the damages observed in the tests discussed in Milani et al. [1]. The experimental campaign mainly focused on an in-scale dry-joint groin vault undergoing the so-called tilting test, i.e. quasi-static rotation of the base platform until failure occurs, resulting in horizontal inertial forces proportional to the mass. The tests investigated the vault behaviour considering the angle ϕ between the tilting axis and one of the symmetry axes of the vault. For the sake of clearness, the damage evolution of the vault with $\phi = 9°$ (quite similar to the one with $\phi = 0°$) is reported in Figure 8. As it is possible to observe, the failure mechanism resulting from limit analysis noticeably matches the experimental one.

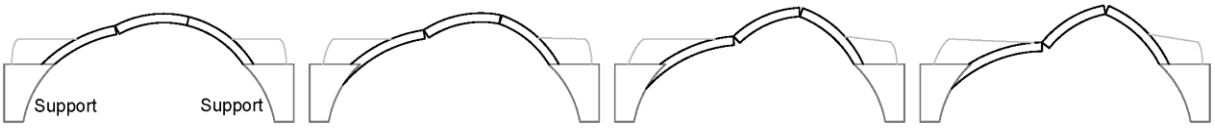

Figure 8. Damage evolution for the groin vault undergoing a tilting test with $\phi = 9°$ from [1]:

perspective sketch of the lateral view

4.2 Range of input parameters

With the aim of defining possible ranges of values in which each mechanism develops, the data have been sorted in form of box-plots, as shown in Figure 9. For each parameter, and according to the already defined mechanisms, the graphs report the quartiles, together with maximum and minimum values, and possible outliers (circles), i.e. values markedly different from the others of the sample. It is worth reminding that, in descriptive statistics, the quartiles of a ranked set of data values are the three points that divide the data set into four equal groups, each group comprising a quarter of the data (e.g. the second quartile is the median of the data). The spacing between the different parts of the box indicates the degree of dispersion.

In reverse, according to the adopted procedure and database, starting from the values of a groin vault, it is possible to assess the most plausible mechanism, or more than one in case of interval overlapping (the most conservative result is recommended). In this regard, in order to deal with *in situ* measurements, the following quantities are considered hereinafter (refer to Figure 10):

S	span (the only geometrical parameter considered as a dimensional quantity [m])
R	rise over span ratio
Th	thickness over span ratio
I	height of the infill over span ratio
f_t	tensile strength [MPa]

For instance, considering a vault with a span S = 4.5 m, rise 1.5 m, thickness 0.20 m, infill up to 60° (1.27 m high above the spring) and null tensile strength, it means R = 0.33, Th = 0.044, I = 0.28, $f_t \approx 0.05$ MPa. Looking at the first line of Figure 9, according to the span dimension, f_t and infill, the vault may fail with a 4H or 2H&R mechanism, or even have a null

seismic capacity. However, considering $R = 0.33$ in the second line of the figure, the mechanism is determined as 2H&R. This result is confirmed in the third line with $Th = 0.044$.

In general, the results for infill equal to 0° and 40° are almost the same, which means that even small amount of debris at the vault corners do not affect the type of collapse failure, at least for static loading. Further findings are collected in Table 3.

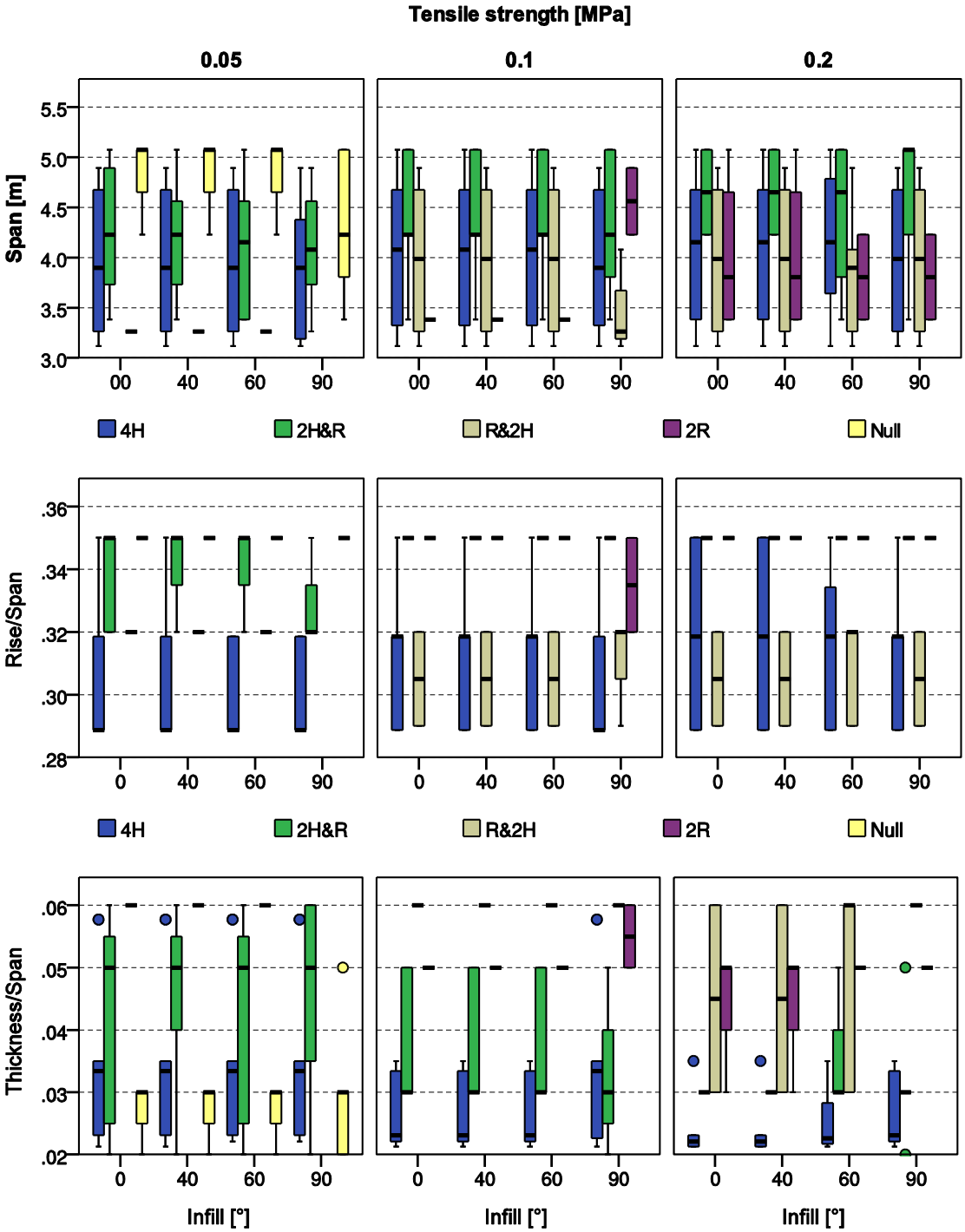

Figure 9. Ranges of the input parameters for most frequent mechanisms (out-of-plane failure)

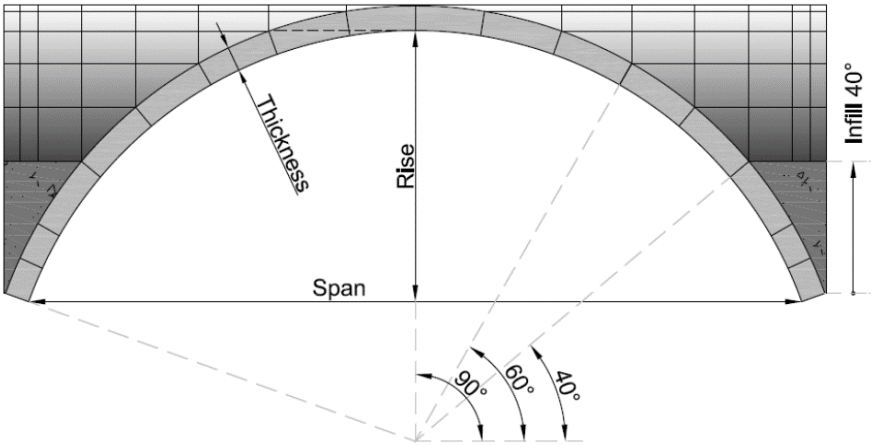

Figure 10. Groin vault geometrical description

	***S* = [3.12, 5.07] m**	***R* = [0.29, 0.35]** (from shallow to high-rise vaults)	***Th* = [0.020, 0.060]** (from thin to thick vaults)
4H	[3.12, 5.07] with a very slight reduction if infill is 90°	[0.29, 0.35] Larger f_t, larger R Larger infill, lower R	[0.021, 0.035] except for isolated cases (corresponding to min R)
2H&R	[3.38, 5.07]	[0.32, 0.35] if f_t =0.05 MPa. R=0.35 with larger f_t	[0.020, 0.060] if f_t =0.05MPa, lower values for larger f_t
R&2H	[3.12, 4.89]	[0.29, 0.32]	Generally, Th=0.060. If f_t =0.20 MPa and infill up to 60°, Th = [0.030, 0.060]
2R	[3.26, 3.38] if f_t =0.05 and 0.10MPa, except one isolated case. [3.38, 5.07] if f_t =0.20MPa, lower values for larger infill	R=0.32 if f_t =0.05MPa R=0.35 if f_t =0.10 and 0.20MPa (except one outlier)	Th=0.060 if f_t =0.05MPa Th=0.050 if f_t =0.10 and 0.20MPa (except few outliers)
Null	[4.23, 5.07] except two isolated cases with infill 90° where S=3.38	R=0.35	Th < 0.030, except one isolated case with infill 90° where Th=0.050

Table 3. Variation of the input parameters for most frequent mechanisms (out-of-plane failure). The ranges of values are reported in the brackets.

In order to have a qualitative understanding regarding the occurrence of the mechanisms, Figure 11 reports the number of times that they developed according to the input parameters. From the first two charts it is clearly visible that the span *S* and height of infill *I* do not produce significant changes in terms of number of occurrences, unless for the null capacity, which is more frequent with larger span. Moreover, as stressed above, the results with infill 0° and 40° are practically the same.

Considering the rise *R*, only 4H and R&2H are associated to a value of 0.29 (shallower vault). On the other hand, if *R*=0.35 (the highest vaults of the database), R&2H never occurred. *R*=0.35 is also the single value which leads to vaults with null capacity. Generally, increasing *R* (that is, from shallow to high-rise vaults), the occurrence of 4H decreases, unlike 2H&R and 2R which increases.

Regarding the thickness, moving from thin to thick vaults, the occurrence of 4H decreases whereas 2H&R and R&2H's increases. Moreover, the value *Th*=0.02 leads to only two mechanisms (and vaults with null capacity), namely 4H and 2H&R, with a strong prevalence of the former. Furthermore, with the highest values of *Th*, almost all the vaults have a capacity larger than zero and a significant occurrence of 2R is now notable.

Finally, regarding the tensile strength, the lowest value (0.05 MPa) does not lead to R&2H but, as expected, it is the only one that leads to null capacity vaults. Increasing the strength, two trends can be observed, namely 2H&R (decreasing), and 2R and R&2H (increasing). The mechanism 4H does not present any significant variation.

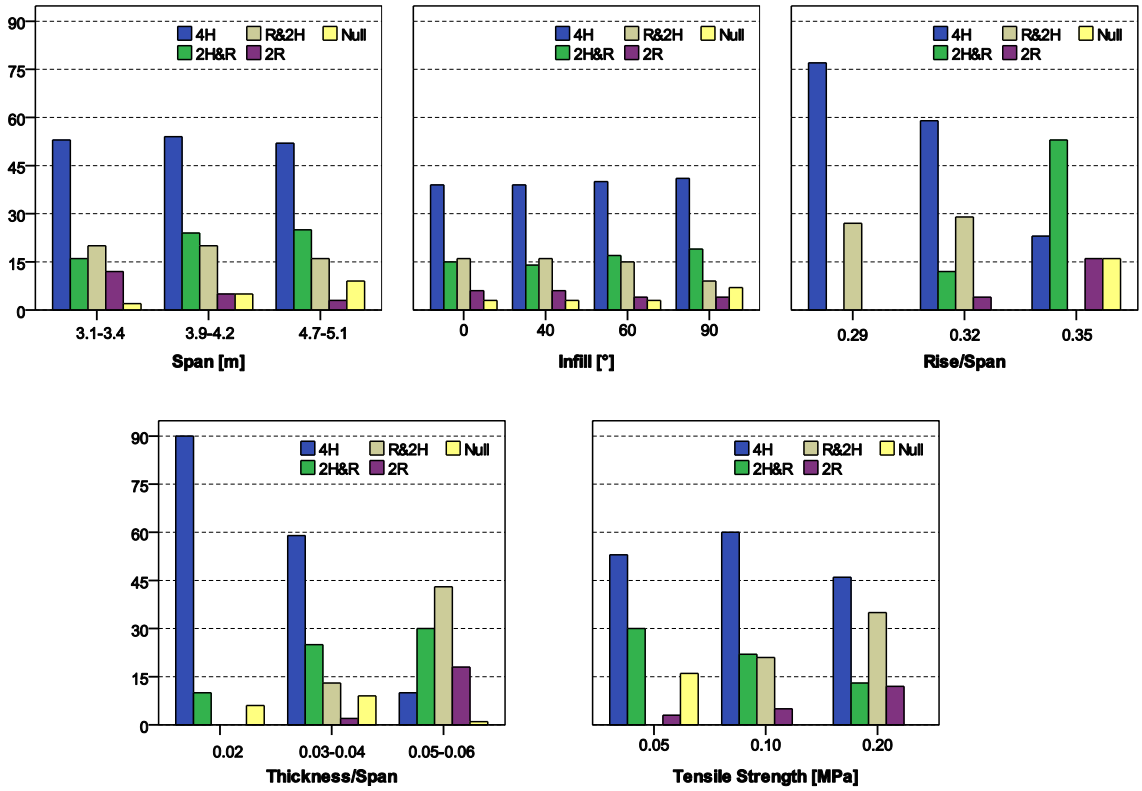

Figure 11. Frequency of the most frequent mechanisms according to the input parameters

(out-of-plane failure)

The comparison in terms of load multiplier (λ) is reported in Figure 12. In general, the capacity of the vault decreases as the span, the infill and the rise increase. On the other hand, it is possible to catch an inverse relationship with the tensile strength. Regarding the thickness, there is a positive relation in case of 4H and 2H&R, whereas it is negative in case R&2H and 2R are considered. Regarding the horizontal load multiplier λ associated to each mechanism, 2H&R provided the lowest range (up to 0.87) whereas 4H and 2R set upon medium ones (a wider interval for the former). R&2H, instead, got values of λ notably larger within [0.90, 2.64].

In general, given the clear trend associated to rise and tensile strength, according to the database considered, these parameters can be assumed as the most crucial in determining the capacity of groin vaults undergoing out-of-phase actions.

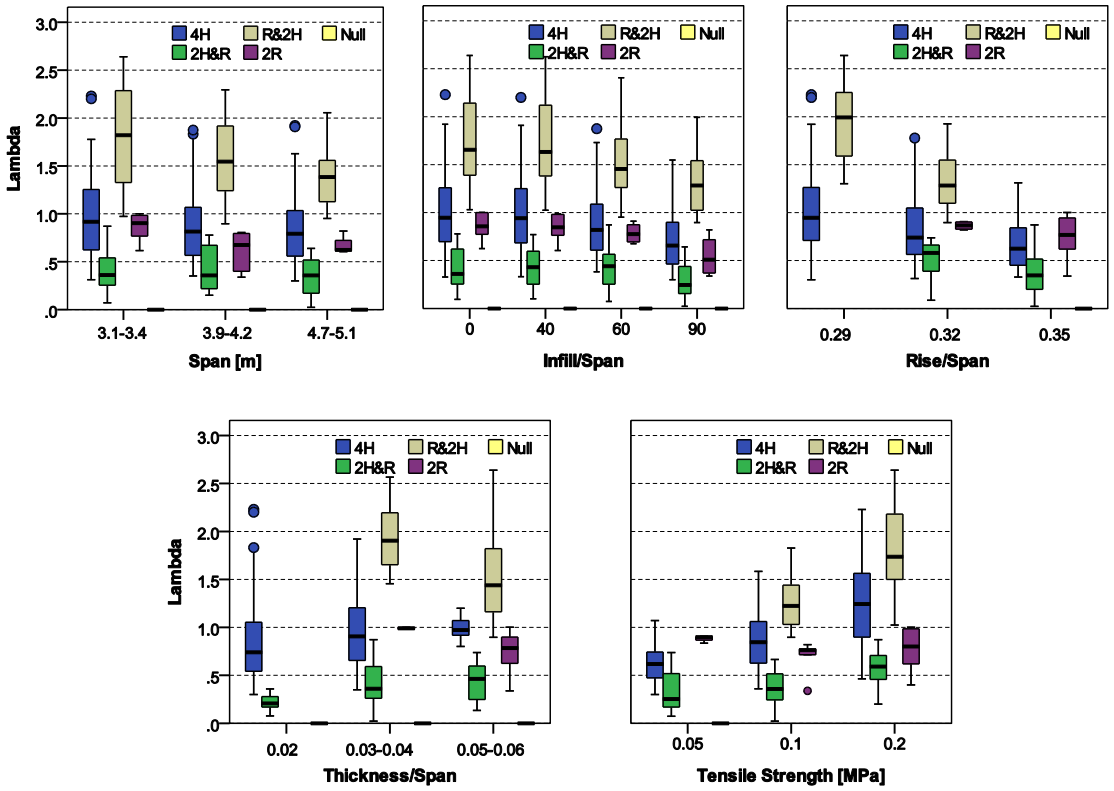

Figure 12. Variation of the load multiplier according to the most frequent mechanisms and the input parameters (out-of-plane failure)

4.3 Multiple linear regression analysis (MLR)

Although the analyses are not time-consuming and results can be obtained without prohibitive computational efforts, simple analytical equations fitted on the outcomes of limit analysis represent an attractive procedure toward a professional-oriented seismic assessment criterion.

In this regard, multiple linear regression (MLR) is a very well-known technique which allows finding (linear) relations between dependent and independent variables (predictors), that are the load multiplier λ and the input parameters, respectively. In order to apply MLR, a linear relation between the predictors and λ is assumed, i.e. first order relation. The general prediction formula is reported in Equation (9). In the following, the estimated values will be indicated with an overline. For instance, the value from the limit analysis is labelled as λ whereas the one from the regression model as $\bar{\lambda}$:

$$\bar{\lambda}_k = \bar{\beta}_0 + \sum_{i=1}^{p} \bar{\beta}_i x_{ki} \qquad k = 1 \dots n$$

$$\bar{\boldsymbol{\lambda}} = \boldsymbol{X}\bar{\boldsymbol{\beta}}$$

$$\bar{\boldsymbol{\lambda}} = \begin{bmatrix} \bar{\lambda}_1 \\ \bar{\lambda}_2 \\ \vdots \\ \vdots \\ \bar{\lambda}_n \end{bmatrix} \qquad \bar{\boldsymbol{\beta}} = \begin{bmatrix} \bar{\beta}_0 \\ \bar{\beta}_1 \\ \vdots \\ \vdots \\ \bar{\beta}_p \end{bmatrix} \qquad \boldsymbol{X} = \begin{bmatrix} 1 & x_{11} & x_{12} & \dots & x_{1p} \\ 1 & x_{21} & x_{22} & \dots & x_{2p} \\ \vdots & \vdots & \vdots & & \vdots \\ \vdots & \vdots & \vdots & & \vdots \\ 1 & x_{n1} & x_{n2} & \dots & x_{np} \end{bmatrix} \tag{9}$$

where $\bar{\lambda}$ is the vector of the k observations, $\bar{\boldsymbol{\beta}}$ the vector of the regression coefficients ($\bar{\beta}_0$ is the intercept at the origin), $\boldsymbol{X}$ is the design matrix with p predictors, namely S, R, Th, I and f_t (Section 4.2). Regarding the dependence of the load multiplier from the predictors, in order to get rid of less significant parameters, a procedure named Stepwise Regression was adopted. This procedure allows identifying the smallest possible set of predictors with a significance close to the maximum. According to this method, given a set of independent variables, each of

them is evaluated under both forward selection and backward deletion. Shortly, predictors are entered in Equation (9) one at a time only if they meet a statistical criterion (F-test with 5% significance), but they may also be deleted at any step where they no longer contribute significantly to the regression model (F-test with 10% significance).

In order to determine the unknown regression coefficients of $\overline{\boldsymbol{\beta}}$ in Equation (9), the Ordinary Least Square method was applied. This method is based on the minimization of the sum of squared residuals (i.e. the differences between the observed values and the estimated values, λ - $\overline{\lambda}$). The values of the regression coefficients are collected in the following equations, where S and f_t are expressed in [m] and [MPa], respectively, and all the other parameters are dimensionless.

$$\bar{\lambda}_{4H} = 2.58 - 0.17S - 5.91R + 14.24Th - 1.34I + 5.86f_t \quad (10)$$

$$\bar{\lambda}_{2H\&R} = 3.70 - 0.13S - 9.38R + 6.77Th - 0.51I + 3.34f_t \quad (11)$$

$$\bar{\lambda}_{R\&2H} = 7.08 - 0.24S - 17.07R - 1.21I + 5.41f_t \quad (12)$$

$$\bar{\lambda}_{2R} = 1.42 - 0.14S - 0.61I \quad (13)$$

The results of MLR are shown in form of scatter diagrams in Figure 13, where the limit analysis outcomes are reported in abscissa and the predicted values in ordinate, i.e. underestimated values are placed below the bisector. As it is possible to see, the simple relations proposed for determining $\overline{\lambda}$ are in good agreement with the limit analysis results. In the diagrams, the coefficient of determination R^2 is also reported for each model, being considerably high, except for the 2R model for which the poor database did not allow a more accurate prediction.

Considering the example of the previous section (S = 4.5 m, R = 0.33, Th = 0.044, I = 0.28, $f_t \approx$ 0.05 MPa) which led to a 2H&R mechanism, the capacity can be calculated with Equation (11), resulting $\overline{\lambda}$ = 0.34.

Looking at the regression equations, given the large difference of predictors (and relative regression coefficients) in terms of orders of magnitude, with the aim of giving a qualitative

indication on how much they are significant to describe the variation of $\overline{\lambda}$, the standardized regression coefficients are considered. They are obtained standardizing all the variables in the MLR, that is, setting the mean to zero and the standard deviation (SD) to one, conveying thus information in SD units. This means the regression coefficients represent the change in response (in terms of SD) for a change of one SD of a predictor. Although very appealing, this information is strictly connected to the input database and the distribution of independent and dependent variables, that is, the methodology puts in relation the true SD of the variables in the database.

Nevertheless, as the predictors become now dimensionless and of the same scale, it is possible to compare the magnitude of the standardized regression coefficients to see which predictor is more effective in each model, and how their effectiveness changes between the models. All the results are collected in Table 4.

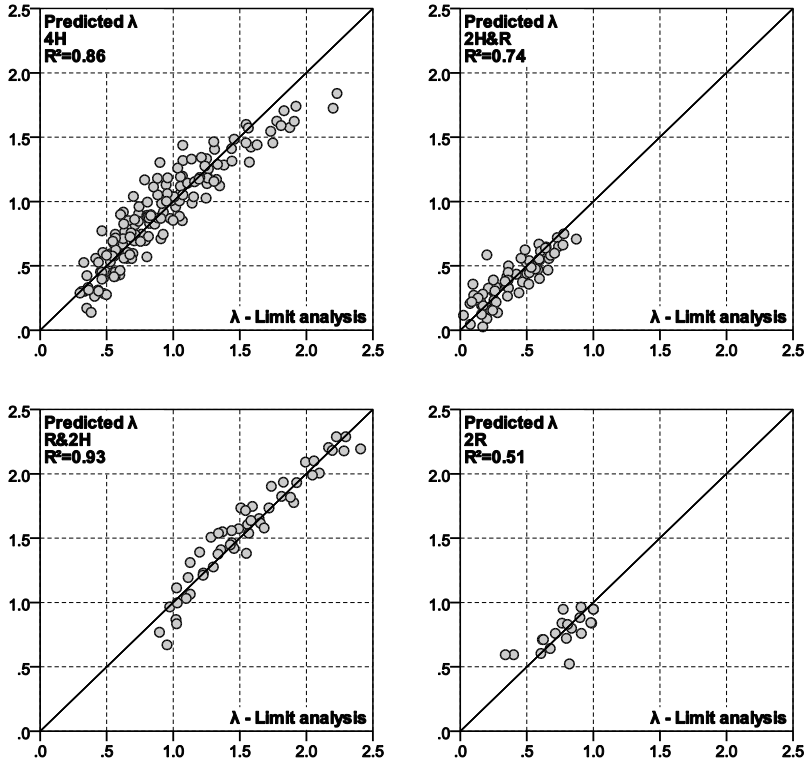

Figure 13. Scatter plots of the prediction models according to MLR (out-of-plane failure)

	Span	Rise/span	Thickness/span	H infill/span	Tensile strength
4H	−0.275	−0.317	0.327	−0.411	**0.860**
2H&R	−0.399	−0.542	0.408	−0.337	**0.883**
R&2H	−0.335	**−0.541**	-	−0.320	**0.558**
2R	**−0.476**	-	-	**−0.478**	-

Table 4. Standardized regression coefficients (out-of-plane failure)

In general, the tensile strength is the most important parameter except for 2R in which its effectiveness is zero. On the other hand, considering R&2H, the rise has the same effectiveness of the tensile strength whereas span and infill play a similar role (the thickness does not contribute). Finally, regarding 2R, only span and infill are involved with an equal importance.

Considering the sign of the regression coefficients, there is always a positive relationship between tensile strength and thickness with respect to the load multiplier, e.g. the larger the thickness, the larger the expected capacity. On the other hand, all the others coefficients show a negative relationship, with the inverse meaning. Moreover, being the only dimensional parameter, the coefficient of the span gives insight on the importance of scale effect, which is crucial in pure sliding mechanism (2R).

5. In-plane shear distortion

This section is similar to the previous one and the reader is referred to it for further explanations. In particular, since the infill schematization *I2* resulted again the most conservative one, only its analysis results are discussed.

5.1 Failure mechanisms

Also in this case, the visual inspection of the resulting 324 analyses (243 with and 81 without infill) indicated the most frequent failure mechanisms that, given the wide range of the input parameters, can be regarded as the most plausible ones for the in-plane shear distortion. However, as stressed above, the mechanisms were clear only with larger values of tensile strength and different cases occasionally showed common features.

The results are collected in Table 5 together with the occurrence frequency. Given the three-dimensional behaviour of the vault, a larger amount of mechanisms was detected and only the ones that covered 90% of all the cases will be considered in the following. These ones are

reported magnified in Figure 14 and, looking at the fixed side of the vault, the mechanisms were sorted considering the predominant bending (B) or sliding (S) failure. In particular, sliding failures involve only the portions of vault close to the supports, leaving the rest of the structure almost undamaged. Figure 14 shows also the simplified schematization through SDOF unstable configurations, absent in the case of the mechanism labelled as "diagonal" (D), which results self-explaining.

Mechanisms	**Abbreviation**	**Frequency**
Bending 1	**B1**	30%
Sliding 1	**S1**	12%
Sliding 2	**S2**	10%
Diagonal	**D**	10%
Bending 2	**B2**	9%
Bending 3	**B3**	8%
Null	**Null**	7%
Sliding 3	**S3**	3%
Others	**-**	<10%

Table 5. Mechanism occurrence frequency for groin vaults subjected to in-plane shear distortion

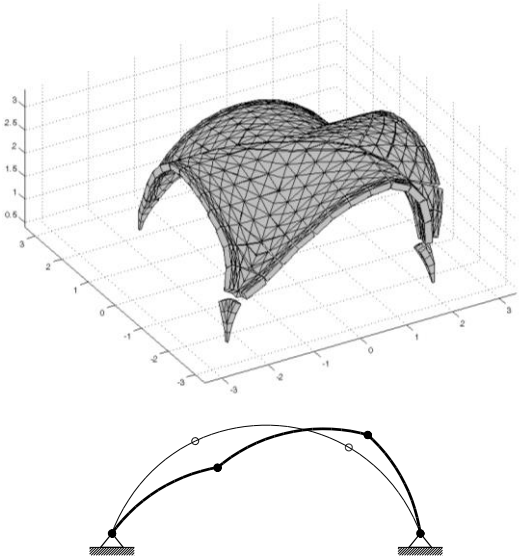

B1

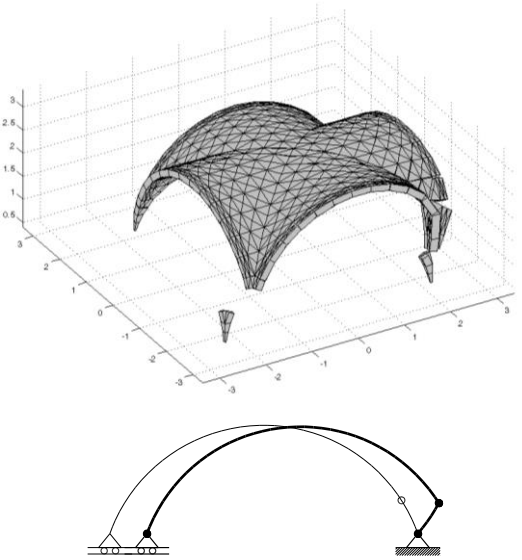

S1

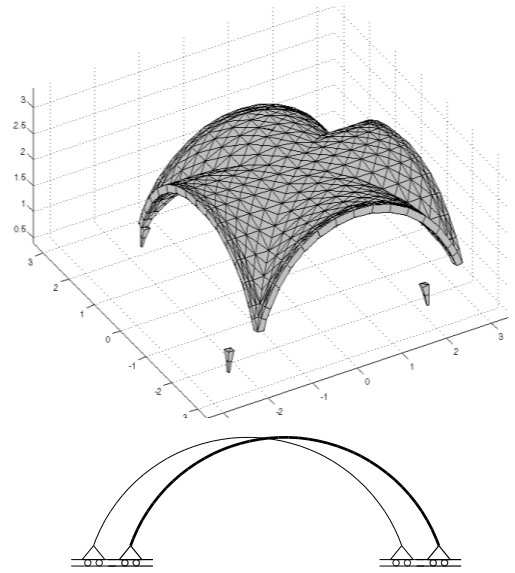

S2

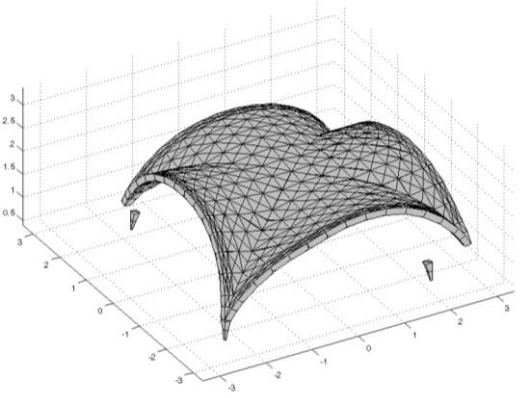

-

D

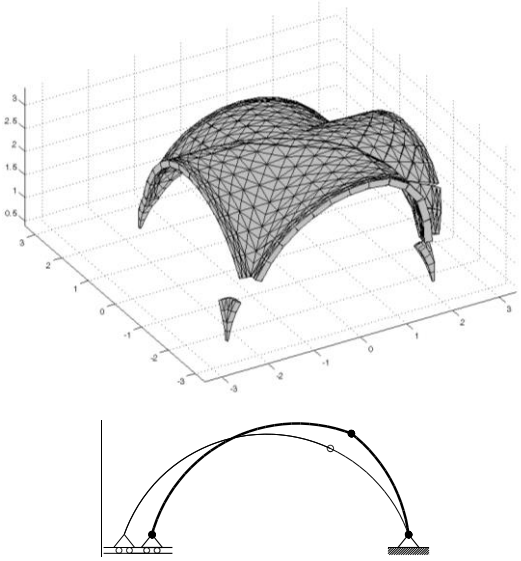

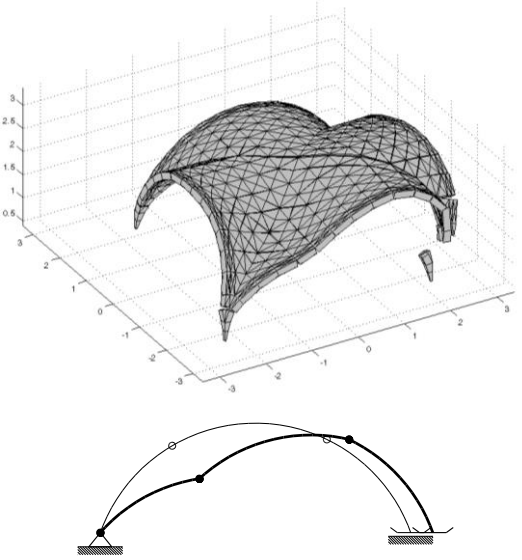

B2 B3

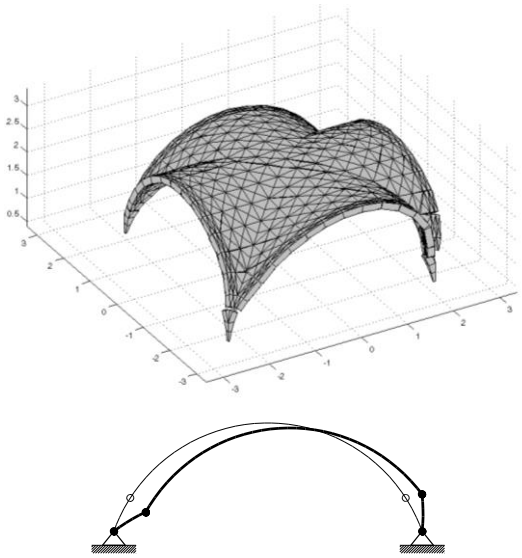

S3

Figure 14. Most frequent mechanisms for in-plane shear distortion and related schematization

5.2 Range of input parameters for each mechanism

All the data were arranged in form of box-plots and reported in Figure 15. As seen in the previous case, for any given set of values referring to an existing vault, it is possible to determine the likely failure mechanism (or more than one in case of overlapping). Again, the results following level of infill equal to 0° and 40° are almost the same, which means that just small amount of debris at the vault corners does not affect the type of failure, at least for static loading.

In general, since the notable difficulty is arising from the three-dimensional behaviour of the vault, only the main findings are reported in Table 6, neglecting the trends based on only a few cases.

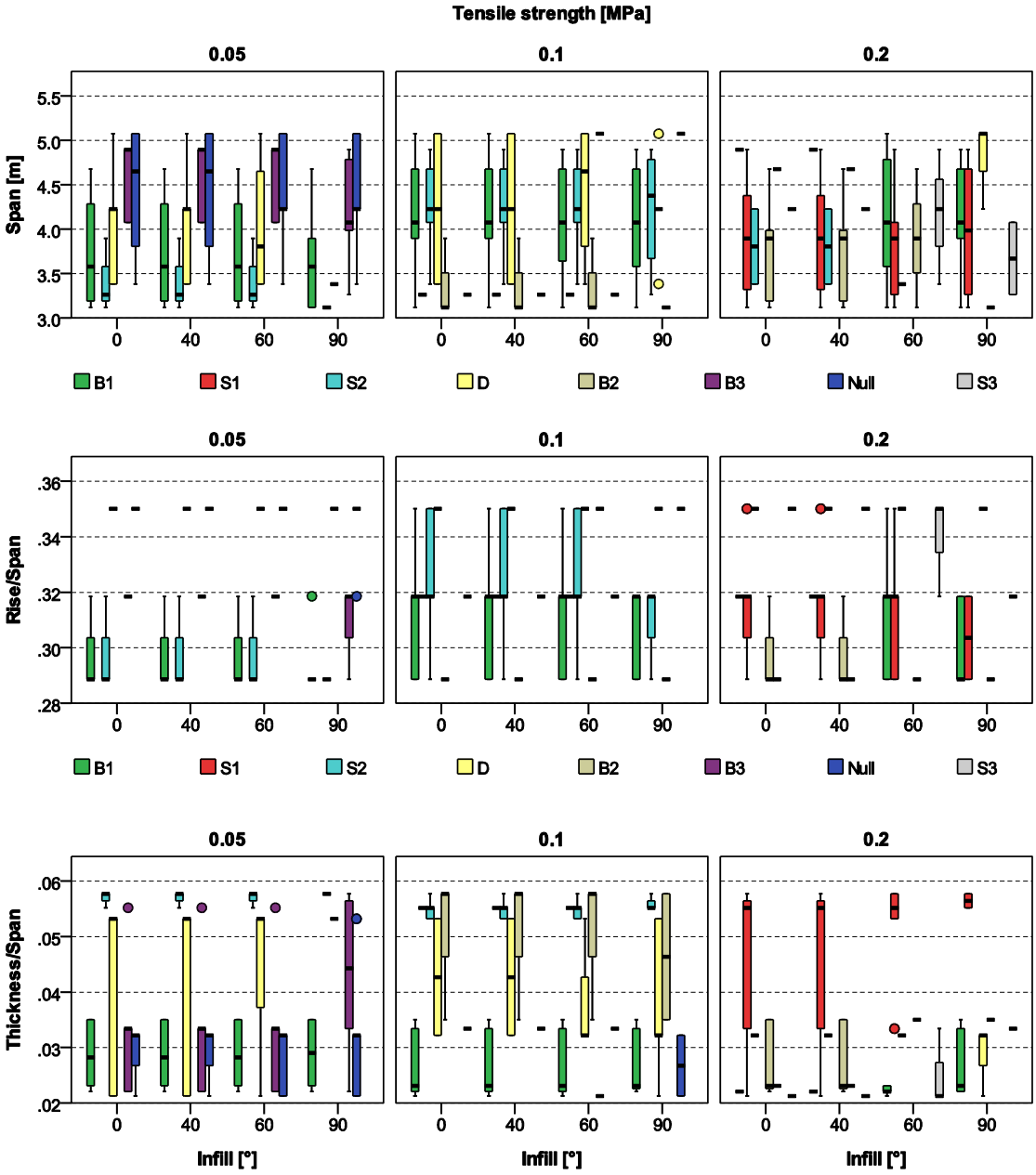

Figure 15. Ranges of the input parameters for most frequent mechanisms (in-plane shear distortion)

	***S* = [3.12, 5.07] m**	***R* = [0.29, 0.35]** (from shallow to high-rise vaults)	***Th* = [0.020, 0.060]** (from thin to thick vaults)
B1	[3.12, 5.07] Lower values if f_t =0.05MPa	Generally within [0.29, 0.32]	[0.021, 0.035]
S1	[3.12, 4.89] Only if f_t =0.20MPa	[0.29, 0.35] generally low values	[0.020, 0.060], larger values for higher infill
S2	[3.12, 3.90] if f_t =0.05MPa [3.26, 4.89] if f_t =0.10MPa [3.38, 4.23] if f_t =0.20MPa	[0.29, 0.35] the larger f_t, the higher rise	[0.053, 0.058] *Th*=0.032 if f_t =0.20MPa
D	[3.38, 5.07] If f_t =0.20, only with infill 90	*R*=0.35	[0.021, 0.053] lower values for larger f_t.
B2	[3.12, 3.90] if f_t =0.10MPa [3.12, 4.68] if f_t =0.20MPa	*R*=0.29 if f_t =0.10MPa [0.29, 0.32] if f_t =0.20MPa	[0.035, 0.058] if f_t =0.10MPa [0.022, 0.035] if f_t =0.20MPa
B3	[3.26, 4.89] lower values if f_t =0.05MPa, and infill 90°	[0.29, 0.32] lower values if f_t =0.05MPa, and infill 90°	[0.020, 0.060] generally higher values if infill is 90°
Null	[3.38, 5.07] if f_t =0.05MPa	*R*=0.32	[0.021, 0.032]
S3	[3.26, 4.89] only if f_t =0.20MPa and infill 60°, 90°	[0.32, 0.35]	[0.021, 0.033]

Table 6. Variation of the input parameters for most frequent mechanisms (in-plane shear distortion). The ranges of values are reported in the brackets.

In order to have a qualitative understanding regarding the occurrence of the mechanisms, Figure 16 reports the number of times that the mechanisms developed according to the input parameters. The increment of the span does not produce significant changes, unless for B2 occurrence, which decreases, and B3 and Null's which increase. Regarding the presence of the infill, the results with infill 0° and 40° are practically the same. Moreover, incrementing the level of the infill (from bare to completely covered vault), S1, S2 and B2 occurrence decreases, whereas the occurrence of null capacity vaults increases.

Considering the rise, from shallow to high-rise vault, only B1 and B2 show a decreasing trend. S1 and B3 have a maximum in frequency in the mid-size vault, whereas D and Null are present only in the highest vault. Regarding the thickness, moving from a thin to thick vault, two clear trends are identifiable: B1 decreases whereas S1 and S2 increases. Null and S3 are basically present only in medium-small thickness vaults, and D and B3 have a minor variation, increasing and decreasing respectively. Finally, looking at the material properties, Null and B3 are present only in case of low f_t, whereas S1, B2 and S3 are present only with higher values, with the occurrence increasing as the f_t increases. D is the only mechanism that decreases as f_t increases, whereas B1 and S2 have a maximum in frequency with the medium value of the tensile strength.

Finally, the comparison in terms of load multiplier (λ) is reported in Figure 17. In general, the capacity of the vault decreases as the infill and the rise increase. On the other hand, it is possible to catch an inverse relationship with the tensile strength. Regarding the other parameters, there are no appreciable trends. However, in general, according to the obtained database and this boundary condition, the groin vaults with R=0.35 and f_t =0.05MPa lead to a horizontal load multiplier lower than 0.8, whereas the largest values can be reached only with S1 and B2 mechanisms.

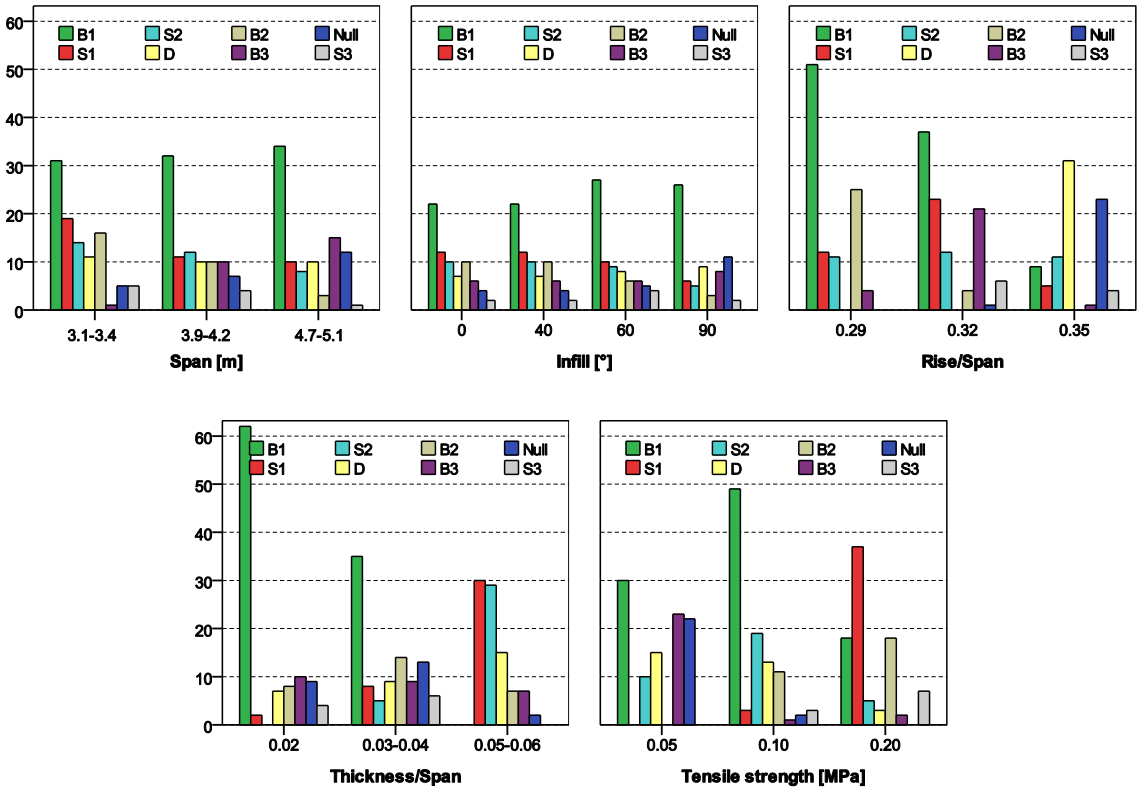

Figure 16. Frequency of the most frequent mechanisms according to the input parameters

(in-plane shear distortion)

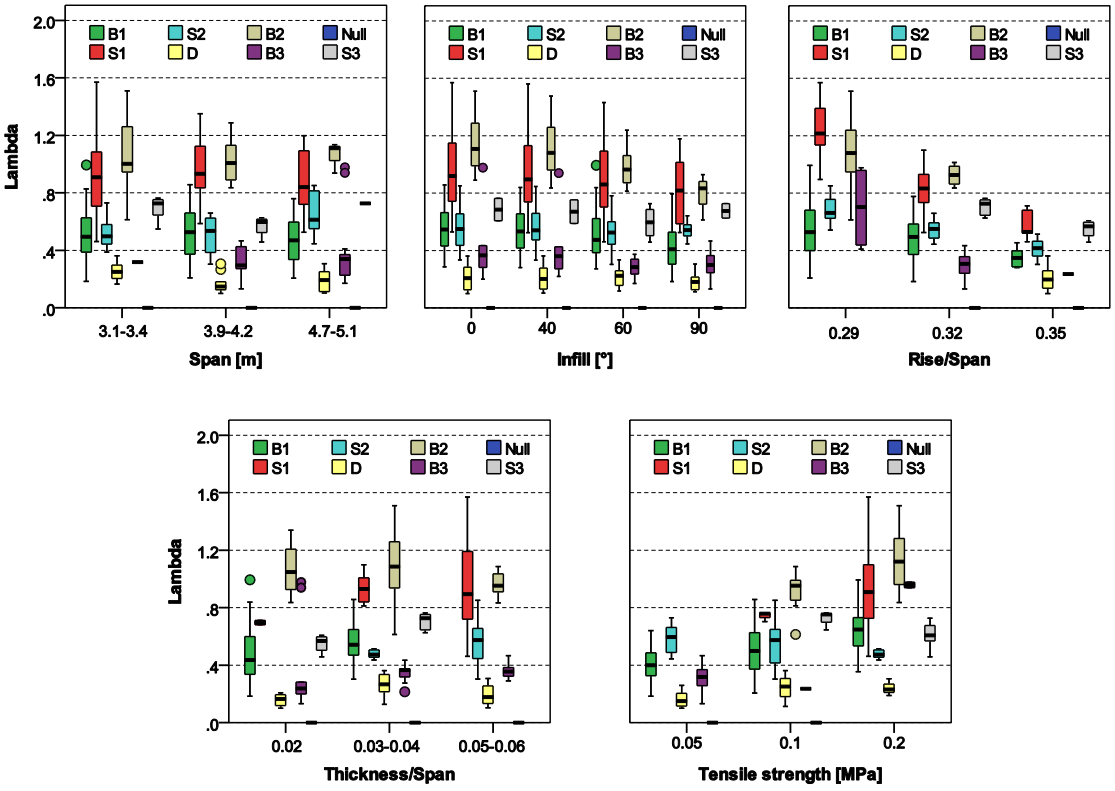

Figure 17. Variation of the load multiplier according to the most frequent mechanisms and the input parameters (in-plane shear distortion)

5.3 Multiple linear regression analysis

According to what described in Section 4.3, the results of MLR are reported in form of scatter diagrams in Figure 18, whereas the values of the regression coefficients are collected in the following equations, where S and f_t are measured in [m] and [MPa], respectively, and all the other parameters are dimensionless:

$$\bar{\lambda}_{B1} = 1.06 - 0.09S - 2.23R + 12.72Th - 0.82I + 2.93f_t \quad (14)$$

$$\bar{\lambda}_{S1} = 5.83 - 0.18S - 13.95R - 3.68Th - 0.70I + 2.34f_t \quad (15)$$

$$\bar{\lambda}_{S2} = 1.54 - 0.07S - 6.27R + 17.24Th - 0.32I + 4.42f_t \quad (16)$$

$$\bar{\lambda}_{D} = 0.36 - 0.08S + 2.40Th - 0.23I + 1.63f_t \quad (17)$$

$$\bar{\lambda}_{B2} = 3.23 - 0.18S - 8.30R + 7.96Th - 1.03I + 4.46f_t \quad (18)$$

$$\bar{\lambda}_{B3} = 1.31 - 0.07S - 3.07R + 4.28Th - 0.36I + 3.86f_t \quad (19)$$

$$\bar{\lambda}_{S3} = 0.32 + 13.80Th - 0.32I \quad (20)$$

As it is possible to see in Figure 18, the simple relationships proposed for determining $\bar{\lambda}$ are in good agreement with the limit analysis results. The coefficient of determination R^2 is also reported in the diagrams, being rather high except for the D mechanism (with values of load multiplier lower than 0.4).

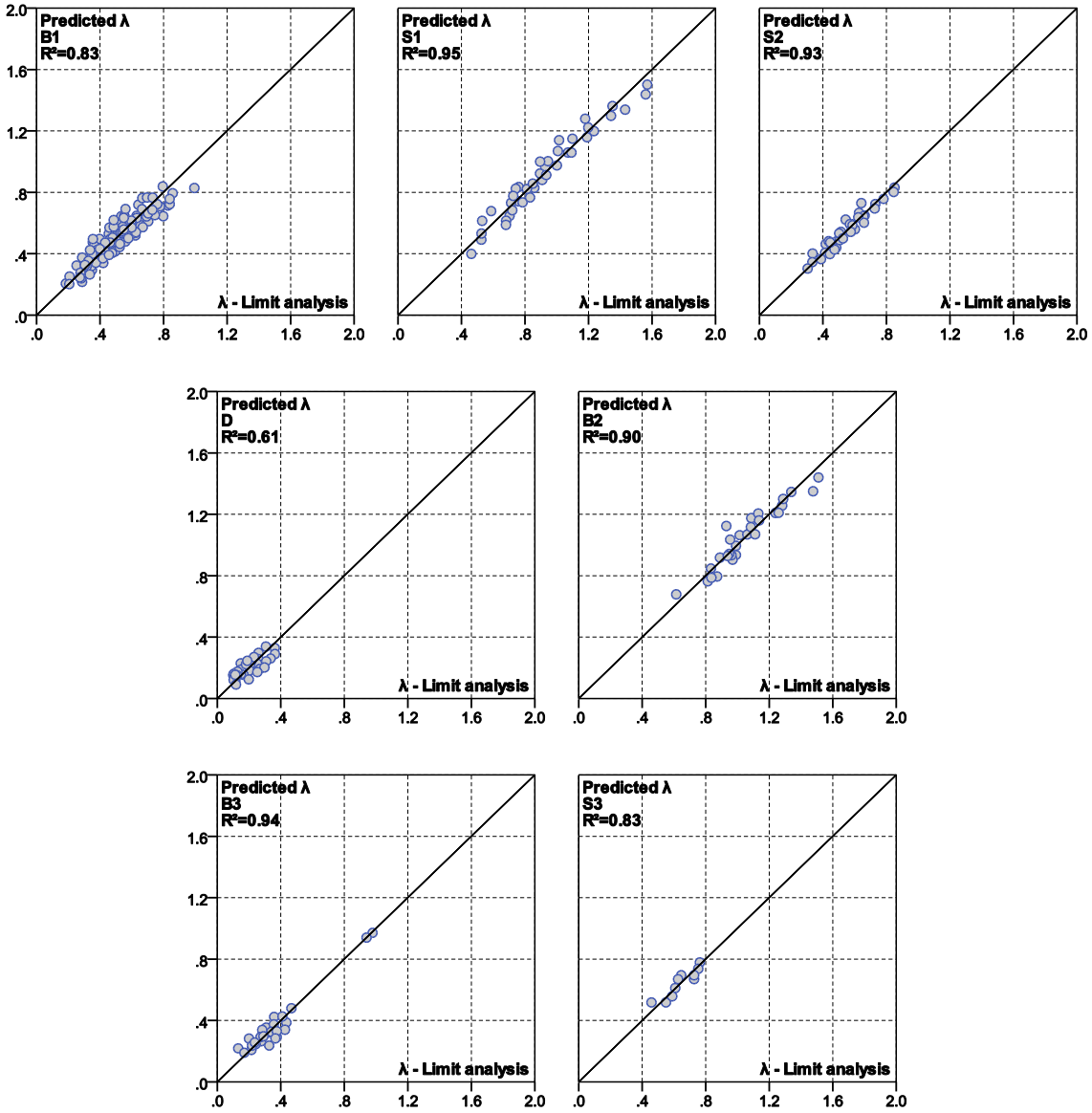

Figure 18. Scatter plots of the prediction models according to MLR (in-plane shear distortion)

For the example examined in of the previous case (S = 4.5 m, R = 0.33, Th = 0.044, I = 0.28, $f_t \approx 0.05$ MPa), the possible mechanisms are D and B3 (Figure 15), which, according to Equations (17) and (19), lead to a load multiplier equal to 0.12 and 0.26, respectively (it is advisable to accept the most conservative value).

Considering the standardized regression coefficients, all the results are collected in Table 7. In general, the tensile strength is always the most important parameter except for S1 and S3, in which the rise and the thickness are the most important parameters, respectively. On the other hand, the rise plays a significant role in S1 and S2. The span and the infill have no decisive roles. Finally, S3, although based on few cases, is governed exclusively by thickness and infill.

Looking at the overall trend between the models, all the coefficients are positive for tensile strength and thickness (except for S1), thus the larger they are, the larger the capacity. On the other hand, all the other coefficients are negative with the inverse meaning. Moreover, as expected, when the stresses are considered, the scale effect is an important issue highlighted by the coefficients of the span, which is the only dimensional parameter.

	Span	Rise/span	Thickness/span	H infill/span	Tensile strength
B1	−0.357	−0.262	0.434	−0.585	**0.886**
S1	−0.413	**−0.963**	−0.148	−0.312	0.222
S2	−0.325	**−1.131**	**1.069**	−0.294	**1.518**
D	−0.711	-	0.410	−0.412	**0.919**
B2	−0.476	−0.428	0.509	−0.551	**1.085**
B3	−0.167	−0.205	0.301	−0.247	**0.815**
S3	-	-	**0.871**	−0.417	-

Table 7. Standardized regression coefficients (in-plane shear distortion)

6. Conclusions

A parametric study on the seismic behaviour of masonry groin vaults was presented. The study was aimed at giving a first contribution to the analysis of the seismic behaviour of masonry cross vaults, still poorly analysed in scientific literature and neglected in the current Codes of Practice. The investigation was performed using a limit analysis-based software considering a wide range of input parameters, namely, span, rise, thickness, infill presence and two boundary conditions.

The first investigation regarded the infill. This was modelled as a distributed load and mass on the extrados of the vault, following four different schematizations. On a safe side perspective, applying the equivalent load of horizontal stripes of infill on both sides of the vault resulted in the most conservative schematization.

The inspection of the parametric analysis outcomes allowed individuating a few main mechanisms for each boundary condition. Four and seven mechanisms were defined, for out-of-plane failure and in-plane shear distortion, respectively. Regarding the former, due to the symmetry of the problem, they resemble the mechanism of a masonry arch undergoing horizontal action. However, the presence of perpendicular webs prompted the inner hinges to be located close to the crown line where the rigidity is minimal. On the other hand, the in-plane shear distortion produced more complicated mechanisms. Possible schematizations were proposed according to the shape of the lateral arch on the fixed side of the vault. Although these results follow from approximate analyses, which need to be validated by experimental evidences and more sophisticated studies, the suggested simple schemes shed light on the structural behaviour of the vault. A possible schematization by means of arch of variable thickness or equivalent arch assemblage may represent a valuable tool for the professional field.

Moreover, according to the two boundary conditions examined, the most influencing parameters were shown, usually represented by tensile strength, thickness and rise, together with possible scale effects. The Multiple Linear Regression analysis provided valuable results for quick assessment of the seismic capacity of groin vaults. In fact, according to reported graphs and the database selected, it is possible to estimate the likely failure mechanism for an existing vault, and calculate the seismic capacity accordingly. More research is needed to take into account uncertainties and to define proper confidence factors.

Finally, the strategy adopted in the present study can be extended to other types of masonry vaulted structures, as different types of cross vault, e.g. with pointed arches, as well as dome and cloister vaults.

Acknowledgements

This work was partly financed by FEDER funds through the Competitivity Factors Operational Programme - COMPETE and by national funds through FCT – Foundation for Science and Technology within the scope of the project POCI-01-0145-FEDER-007633.

References

[1] Milani G, Rossi M, Calderini C, Lagomarsino S. Tilting plane tests on a small-scale masonry cross vault: Experimental results and numerical simulations through a heterogeneous approach. Eng Struct 2016;123:300–12. doi:10.1016/j.engstruct.2016.05.017.

[2] Page AW. The biaxial compressive strength of brick masonry. Proc Inst Civ Eng 1981;71:893–906. doi:10.1680/iicep.1981.1825.

[3] Lourenço PB, Rots JG. Multisurface interface model for analysis of masonry structures. J Eng Mech 1997;123:660–8.

[4] Milani G, Milani E, Tralli A. Upper bound limit analysis model for FRP–reinforced masonry curved structures. Part II: Structural analyses. Comput Struct 2009;87:1534–58. doi:10.1016/j.compstruc.2009.07.010.

[5] NTC. Italian Building Code for the Constructions (Norme Tecniche per le Costruzioni). D. M. 14 January 2008 – S.O. N. 30, G. U. N. 29–4. Italia: 2008.

[6] CM. Instruction for the application of the Building Standard for Constructions 2009.

[7] Eurocode 8. Comite European de Normalization (CEN). Design of Structures for Earthquake Resistance. EN 2004-1-1, Brussels: 2004.

[8] National Civil Protection Service. Manuale per la compilazione della scheda per il rilievo del danno ai beni culturali, chiese - MODELLO A-DC. Ed. by Simona Papa and Giacomo Di Pasquale: 2013.

[9] Lourenço PB. Computations on historic masonry structures. Prog Struct Eng Mater 2002;4:301–19. doi:10.1002/pse.120.

[10] Ceradini V. Modelli sperimentali di volte in tufo e mattoni. La Mecc. delle murature tra Teor. e Progett., Messina: 1996, p. 157–66.

[11] Van Mele T, McInerney J, DeJong M, Block P. Physical and computational discrete modelling of masonry vault collapse. In: Jerzy Jasieńko, editor. Struct. Anal. Hist. Constr., Wrocław: 2012, p. 2552–60.

[12] McInerney J, DeJong M. Discrete Element Modeling of Groin Vault Displacement Capacity. Int J Archit Herit 2015;9:1037–49. doi:10.1080/15583058.2014.923953.

[13] Barthel R. Tragverhalten gemauerter - Kreuzgewölbe. Aus Forsch. und Lehre, No. 26, Karlsruhe: University of Karlsruhe; 1991.

[14] Conde B, Díaz-Vilariño L, Lagüela S, Arias P. Structural analysis of Monforte de Lemos masonry arch bridge considering the influence of the geometry of the arches and fill material on the collapse load estimation. Constr Build Mater 2016;120:630–42. doi:10.1016/j.conbuildmat.2016.05.107.

[15] LimitState Ltd. LimitState:Ring Manual 2016.

[16] Gago AS, Alfaiate J, Lamas A. The effect of the infill in arched structures: Analytical and numerical modelling. Eng Struct 2011;33:1450–8. doi:10.1016/j.engstruct.2010.12.037.

[17] Gaetani A, Monti G, Lourenço PB, Marcari G. Design and Analysis of Cross Vaults

Along History. Int J Archit Herit 2016;10:841–56. doi:10.1080/15583058.2015.1132020.

[18] Rossi M, Calderini C, Lagomarsino S. Experimental testing of the seismic in-plane displacement capacity of masonry cross vaults through a scale model. Bull Earthq Eng 2015. doi:10.1007/s10518-015-9815-1.

[19] Mouzakis H, Adami CE, Karapitta L, Vintzileou E. Seismic behaviour of a rehabilitated cross vault. In: Jasieńko J, editor. Struct. Anal. Hist. Constr., Wrocław: 2012, p. 1665–73.

[20] Theodossopoulos D, Sinha BP, Usmani AS, Macdonald AJ. Assessment of the structural response of masonry cross vaults. Strain 2002;38:119–27. doi:10.1046/j.0039-2103.2002.00021.x.

[21] Doglioni F, Moretti A, Petrini V, (Ed. by). Le chiese e il terremoto. Dalla vulnerabilità constatata nel terremoto del Friuli al miglioramento antisismico nel restauro. Verso una politica di prevenzione. Trieste: Lint Editoriale Associati; 1994.

[22] Regione Toscana. Istruzioni tecniche per l'interpretazione ed il rilievo per macroelementi del danno e della vulnerabilità sismica delle chiese. Venzone: ARX s.c.r.l.; 2003.

[23] Podestà S, Brignola A, Curti E, Parodi S, Lemme A. Damage assessment and seismic vulnerability of churches: the Abruzzo earthquake. Ing Sismica 2010;XXVII:21–35.

[24] Gilbert M. RING: A 2D rigid block analysis program for masonry arch bridges. 3rd Int. Arch Bridg. Conf., Paris: 2001, p. 109–18.

[25] Cavicchi A, Gambarotta L. Collapse analysis of masonry bridges taking into account arch–fill interaction. Eng Struct 2005;27:605–15. doi:10.1016/j.engstruct.2004.12.002.

[26] Cavicchi A, Gambarotta L. Two-dimensional finite element upper bound limit analysis of masonry bridges. Comput Struct 2006;84:2316–28. doi:10.1016/j.compstruc.2006.08.048.

[27] Milani G, Lourenço PB. 3D non-linear behavior of masonry arch bridges. Comput Struct 2012;110–111:133–50. doi:10.1016/j.compstruc.2012.07.008.

[28] Croci G. General methodology for the structural restoration of historic buildings: the cases of the Tower of Pisa and the Basilica of Assisi. J Cult Herit 2000;1:7–18. doi:10.1016/S1296-2074(99)00119-3.

[29] Milani G, Milani E, Tralli A. Upper Bound limit analysis model for FRP-reinforced masonry curved structures. Part I: Unreinforced masonry failure surfaces. Comput Struct 2009;87:1516–33. doi:10.1016/j.compstruc.2009.07.007.

[30] Krabbenhoft K, Lyamin A V., Hjiaj M, Sloan SW. A new discontinuous upper bound limit analysis formulation. Int J Numer Methods Eng 2005;63:1069–88. doi:10.1002/nme.1314.

[31] Wolsey LA. Integer programming. New York: John Wiley and Sons; 1998.

[32] Chvatal V. Linear Programming. New York: W.H. Freeman and Company; 1983.

[33] Clemente P. La verifica degli archi a conci lapidei. ENEA, Unità comunicazione e informazione; 1997.